Cubic scaling algorithm for the random phase approximation: Self-interstitials and vacancies in Si

Merzuk Kaltak, Jiří Klimeš, and Georg Kresse[*]

University of Vienna, Faculty of Physics and Center for Computational Materials Science, Sensengasse 8/12, A-1090 Vienna, Austria

The random phase approximation (RPA) to the correlation energy is among the most promising methods to obtain accurate correlation energy differences from diagrammatic perturbation theory at modest computational cost. We show here that a cubic system size scaling can be readily obtained, which dramatically reduces the computation time by one to two orders of magnitude for large systems. Furthermore, the scaling with respect to the number of k points used to sample the Brillouin zone can be reduced to linear order. In combination, this allows accurate and very well-converged single-point RPA calculations, with a time complexity that is roughly on par or better than for self-consistent Hartree-Fock and hybrid-functional calculations. The present implementation enables new applications. Here, we apply the RPA to determine the energy difference between diamond Si and β-tin Si, the energetics of the Si self-interstitial defect and the Si vacancy, the latter with up to 256 atom supercells. We show that the RPA predicts Si interstitial and vacancy energies in excellent agreement with experiment. Si self-interstitial diffusion barriers are also in good agreement with experiment, as opposed to previous calculations based on hybrid functionals or range-separated RPA variants.

PACS number(s): 71.15.Nc, 71.15.Dx, 71.55.Gs

I. INTRODUCTION

The random phase approximation (RPA) is presently one of the most promising routes to improve upon conventional local or semilocal density functionals [1]. It yields a rather good and balanced description of most bonding types, including metallic bonding, covalent, ionic, and, maybe most importantly, van der Waals (vdW) bonding. Initial applications were limited to small molecules [2], but first applications to bulk materials followed soon [3]. The initial results were, however, not particularly encouraging with lattice constants and binding energies generally worse than for standard density functionals. Only when improved implementations, extrapolation to the infinite-basis-set limit, and relative energies between chemically relevant entities were considered, results often surpassed that for semilocal functionals [4–7]. The studies now span a wide range of applications, including molecular reactions [8], rare gas solids [5], properties of covalent, metallic, and ionic solids [9–13], dispersion forces in graphite and between graphene and surfaces [14–16], layered compounds [17], adsorption of molecules on surfaces [18], bulk ice properties [19], and many more applications are emerging.

Conventional local or semilocal density functionals only describe covalent, metallic, and ionic bonding correctly, or one should rather say "reasonably" accurately. However, all local approximations will necessarily fail for dynamic dipole-dipole interactions. Schemes to add nonlocal dynamic correlation effects (van der Waals–type bonding) are currently an active research field. These include atom-centered dispersion corrections [20–23] as well as nonlocal van der Waals corrections considering the density at two points in space [24–28]. But, none of these approaches are as seamless as the random phase approximation. For instance, the random phase approximation sets out from the exact exchange (EXX) energy and adds correlation on top, whereas the semiempirical van

der Waals corrections all need to rely on a more approximate description of the exchange, usually conventional semilocal density functionals or hybrid functionals.

There is no denying that RPA is not perfect. Among all the possible many-body diagrams that should be included, direct RPA exclusively sums the bubble diagrams. Attempts to include other kind of diagrams, for instance, higher-order exchange interactions [29,30], the contribution of single excitations [31–34] or approximate exchange and correlation contributions inspired by density functional theory [35] are currently vigorously explored research directions. Also, better starting points than standard density functionals are explored [36,37]. Likewise, forces are yet only implemented in two molecular codes [38,39], and they are not available in solid-state codes.

Another obstacle of the random phase approximation is that even the most efficient implementations are presently scaling with the fourth power of the system size M (i.e., M^4), and related to this, the time complexity also increases quadratically with the number of k points that are used to sample the Brillouin zone. Hence, calculations are limited to, by today's standards, small system sizes, typically 50–100 atoms and very few k points, or even smaller systems with 10–20 atoms and at most 100 k points. But, such calculations can require days or even weeks on modern high-performance computers.

A solution to this problem has been suggested about two decades ago by Godby and co-workers in the context of the GW approximation [40,41]. In the RPA and GW approximation, the computationally most demanding step is the calculation of the independent-particle response function at a set of imaginary frequencies [42,43]. At each frequency, the calculation of the response function involves a summation over all pairs of occupied and unoccupied states ($N_o N_u$), with a rank-one update of the microscopic response function for each pair (scaling quadratically with number of basis functions N_b). Overall, this yields the previously described scaling. There is one, in principle, exact alternative that avoids this unfavorable

*georg.kresse@univie.ac.at

scaling. Calculate the Green's function of the occupied states $\underline{G}$ ($N_o N_b^2$) and likewise the Green's function of the unoccupied states $\overline{G}$ (scaling like $N_u N_b^2$) and determine the response function by contraction over the two functions. This step is ideally performed at a set of imaginary-time points. The problem that then needs to be addressed is the transformation from the imaginary time to the imaginary frequency using a minimum set of time and frequency points. All previous implementations of this approach relied on a combination of interpolations, analytic continuations, and standard Fourier transformations using uniform grids. In a recent work, the present authors derived an efficient discrete Fourier transform that allows us to achieve μeV accuracy per atom with as few as 16 time and frequency points [44]. An alternative favorably scaling approach was recently discussed by Moussa [45].

In this paper, a detailed discussion of the favorably scaling RPA implementation is presented for the projector augmented wave (PAW) method at finite k-point sampling in Sec. II. After briefly discussing results for bulk Si (Sec. IV A), we show that the present approach can be applied to 64 atoms and rather accurate $3 \times 3 \times 3$ k-point grids, or 216 atoms and up to 4 k points (Sec. IV B). In both cases, the required computation time is a few hours on 128 cores. Using the present approach, we calculate the Si self-interstitial energies and Si monovacancy formation energy and compare to previous results in Sec. IV C. The comparison with experiment and diffusion Monte Carlo suggests that the RPA yields excellent results. Furthermore, the present results agree well with vdW corrected hybrid-functional calculations, validating these calculations [22].

II. THEORY

In this section, we discuss the basic steps for the computation of the correlation energy in the random phase approximation E^{RPA}. In the random phase approximation, the correlation energy is given by [1,46]

$$E^{\text{RPA}} = \int_0^\infty \frac{d\omega}{2\pi} \, \text{Tr} \left\{ \ln \left[1 - \chi(i\omega)\nu \right] + \chi(i\omega)\nu \right\}. \quad (1)$$

Here, χ is the independent-particle polarizability on the imaginary frequency axis and ν represents the Coulomb interaction. The trace Tr in Eq. (1) is evaluated most efficiently in the reciprocal space and is discussed elsewhere [5].

However, this is only the final step in the full RPA algorithm shown schematically in Fig. 1. We discuss the individual steps separately in the following subsections, starting with a discussion of the chosen frequency grid and the evaluation of the cosine transformation from the imaginary time to the imaginary frequency axis.

A. Imaginary-time and frequency grids: The sloppy cosine transformation

The frequency integration in Eq. (1) is evaluated by a numerical quadrature and discussed in detail in Ref. [44]. Here, we summarize only the main points. The frequency and time grids are obtained by minimizing the discretization error of the leading contribution to E^{RPA}, the direct Møller-Plesset energy
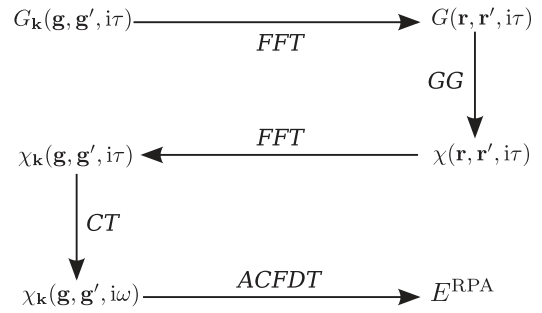

FIG. 1. Calculation scheme for the RPA correlation energy E^{RPA} adopted in this paper. The first and third steps are a spatial fast Fourier transformation (FFT) described in Sec. II B. The second step is the contraction of two Green's functions in the space-time domain (GG) giving the independent-particle polarizability χ (see Sec. II C). The cosine transformation (CT) in the fourth step is described in Sec. II A. The adiabatic connection fluctuation dissipation theorem (ACFDT) is formulated in Eq. (1).

in second order [47,48]

$$E^{(2)} = -\int_0^\infty \frac{d\omega}{4\pi} \text{Tr}([\chi(i\omega)\nu]^2). \quad (2)$$

To obtain a closed expression for the energy, the Adler and Wiser formula for the independent-particle polarizability [42,43]

$$\chi_{\mathbf{k}}(\mathbf{g}, \mathbf{g}', i\omega_k) = \sum_{ia} \xi_{ia}(i\omega_k) \langle \psi_i | e^{i(\mathbf{g}+\mathbf{k})\mathbf{r}} | \psi_a \rangle$$
$$\times \langle \psi_a | e^{-i(\mathbf{g}'+\mathbf{k})\mathbf{r}'} | \psi_i \rangle \quad (3)$$

with the weights

$$\xi_{ia}(i\omega_k) = \frac{2(\epsilon_a - \epsilon_i)}{(\epsilon_a - \epsilon_i)^2 + \omega_k^2} \quad (4)$$

is inserted into Eq. (2). The imaginary frequency integral is carried out analytically yielding

$$E^{(2)} = \frac{1}{2} \sum_{ijab} \frac{|\langle \psi_i \psi_j | \nu | \psi_a \psi_b \rangle|^2}{\epsilon_i + \epsilon_j - \epsilon_a - \epsilon_b}, \quad (5)$$

the conventional direct Møller-Plesset energy expression. In the last expressions, the indices i and j label occupied orbitals with one-electron energies ϵ_i, ϵ_j, and a and b indicate unoccupied orbitals. After discretization of (2) by a quadrature with weights $\vec{\gamma} = (\gamma_1, \ldots, \gamma_{N_\omega})$ and abscissas $\vec{\omega} = (\omega_1, \ldots, \omega_{N_\omega})$, the resulting expression is subtracted from the exact second-order energy Eq. (5). The discretization error is minimized only for the dominating terms with $\epsilon_a = \epsilon_b$ and $\epsilon_i = \epsilon_j$ [44].

This yields an error estimate

$$\eta(x, \vec{\omega}, \vec{\gamma}) = \frac{1}{x} - \sum_{k=1}^{N_\omega} \gamma_k \frac{4x^2}{\left(x^2 + \omega_k^2\right)^2} \quad (6)$$

for each transition energy x in the interval

$$\min(\epsilon_a - \epsilon_i) \leqslant x \leqslant \max(\epsilon_a - \epsilon_i).$$

This error function is minimized with respect to the Chebyshev norm giving the optimum N_ω quadrature points for the evaluation of the RPA correlation energy Eq. (1).

The time grid is constructed analogously using the corresponding imaginary-time representations of Eqs. (3) and (2) yielding the error function [49]

$$\hat{\eta}(x, \vec{\tau}, \vec{w}) = \frac{1}{x} - \sum_{i=1}^{N_\omega} w_i e^{-x\tau_i}. \tag{7}$$

In the RPA algorithm presented in this work, the independent-particle polarizability on the imaginary frequency axis ω_k is determined by a Fourier transformation from the imaginary-time representation $\chi(i\tau_i)$ (see Fig. 1). This is achieved using the nonuniform cosine transformation [44]

$$\chi(i\omega_k) = \sum_{i=1}^{N_\omega} \gamma_{ik} \cos(\omega_k \tau_i) \chi(i\tau_i). \tag{8}$$

The coefficients γ_{ik} are determined in analogy to the time and frequency grid by minimizing the error function

$$\tilde{\eta}(x, \omega_k, \vec{\gamma}) = \frac{2x}{x - \omega_k^2} - \sum_{i=1}^{N_\omega} \gamma_{ik} \cos(\omega_k \tau_i) e^{-x\tau_i} \tag{9}$$

for each frequency point ω_k separately. We have observed that the RPA integral (1) as well as the cosine transformation can be evaluated accurately with a modest number of grid points [44]. Typically, 16 time and frequency points suffice for μeV accuracy per atom.

B. Fast Fourier transforms within supercells

In order to calculate the polarizability efficiently, spatial fast Fourier transformations (FFTs) in steps one and three in Fig. 1 are required. Using supercells allows us to achieve linear scaling with respect to the number of k points in the contraction step GG (discussed in Sec. II C). Before continuing, we review a few basic relations between real and reciprocal space and introduce a concise terminology.

Given a unit cell C, the corresponding first Brillouin zone will be denoted by C^*. We call the set of all translation vectors of the unit cell $\mathcal{L}_c$ and, vice versa, $\mathcal{L}_c^*$ indicates the set of all translation vectors vectors of C^*. The vectors $\mathbf{g} \in \mathcal{L}_c^*$ are the usual reciprocal lattice vectors (large dots in Fig. 2). If the unit cell C is replicated $\mathcal{N}$ times along each direction, a supercell S containing $\mathcal{N}^3$ copies of the original unit cell C is obtained. Then, the corresponding Brillouin zone S^* is a subset of C^*. Their origins, the Γ point, coincide (cf. Fig. 2) [50]. Analogously to the unit cell, we write $\mathcal{L}_s$ and $\mathcal{L}_s^*$ for the translational vector sets of the supercell S. It follows immediately that [50,51]

$$\mathcal{L}_c^* \subseteq \mathcal{L}_s^*. \tag{10}$$

The reciprocal superlattice vectors $\mathbf{G}$ build a uniform $\mathcal{N} \times \mathcal{N} \times \mathcal{N}$ lattice $\mathcal{K}_{c^*}$ containing N_k vectors $\mathbf{k}$ in the first Brillouin zone of the original unit cell C^*. These are the k points (see Fig. 2) used to sample the Brillouin zone in the original primitive computational cell. In the following, we will distinguish between reciprocal superlattice vectors $\mathbf{G} \in \mathcal{L}_s^*$ and the k points $\mathbf{k} \in \mathcal{K}_c^*$.

Quantities such as the response function χ or the Green's function G are periodic in space

$$G(\mathbf{r} + \mathbf{a}, \mathbf{r}' + \mathbf{a}) = G(\mathbf{r}, \mathbf{r}'), \quad \forall \mathbf{a} \in \mathcal{L}_c. \tag{11}$$
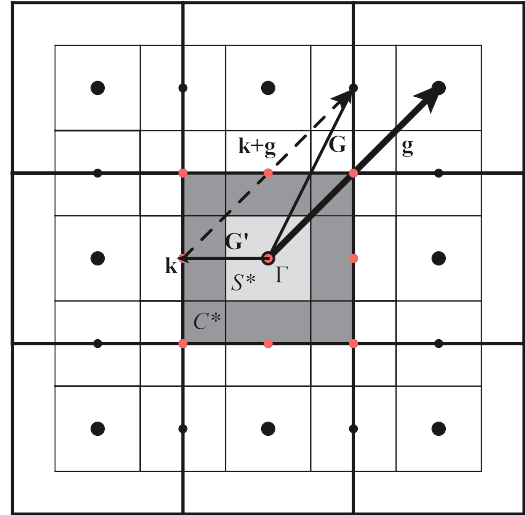

FIG. 2. (Color online) Illustration of relation between reciprocal cell C^* (dark gray cell), k-point grid $\mathcal{K}_c^*$ (red dots in dark gray square), and reciprocal supercell S^* (small light gray square) for a two-dimensional cubic cell with $S = (2 \times 2)C$. The vector $\mathbf{g}$ is a reciprocal lattice vector of C^* and $\mathbf{G}$ is a reciprocal lattice vector of S^*. The set of all reciprocal lattice vectors $\mathcal{L}_c^*$ is represented by big dots and is a subset of $\mathcal{L}_s^*$, the set of all reciprocal superlattice vectors (small and big dots). The k point $\mathbf{k}$ coincides with the reciprocal superlattice vector $\mathbf{G}'$ and every vector $\mathbf{k} + \mathbf{g}$ can be represented by a reciprocal superlattice vector $\mathbf{G}$.

This implies that the Fourier representation of G can be written as [52]

$$G(\mathbf{r}, \mathbf{r}') = \frac{1}{N_k} \sum_{\mathbf{k} \in \mathcal{K}_c^*} G_\mathbf{k}(\mathbf{r}, \mathbf{r}'), \tag{12}$$

where

$$G_\mathbf{k}(\mathbf{r}, \mathbf{r}') = \sum_{\mathbf{g}\mathbf{g}' \in \mathcal{L}_c^*} e^{-i(\mathbf{k}+\mathbf{g})\mathbf{r}} G_\mathbf{k}(\mathbf{g}, \mathbf{g}') e^{i(\mathbf{k}+\mathbf{g}')\mathbf{r}'} \tag{13}$$

and $N_k = \mathcal{N}^3$ denotes the number of k points in the first Brillouin zone of the unit cell. In the last expression, the notation

$$G_\mathbf{k}(\mathbf{g}, \mathbf{g}') = G(\mathbf{k}+\mathbf{g}, \mathbf{k}+\mathbf{g}'), \quad \forall \mathbf{k} \in \mathcal{K}_c^*, \mathbf{g} \in \mathcal{L}_c^* \tag{14}$$

was used, which indicates that for each $\mathbf{k} \in \mathcal{K}_c^*$ a different set of points in the reciprocal space $\mathbf{k}+\mathbf{g}, \mathbf{k}+\mathbf{g}'$ form a matrix $G_\mathbf{k}$ with indices $\mathbf{g}, \mathbf{g}' \in \mathcal{L}_c^*$. We note that for each $\mathbf{k}$, the set $\{\mathbf{k}+\mathbf{g}\}_{\mathbf{g} \in \mathcal{L}_c^*}$ covers a different subset of $\mathcal{L}_s^*$, so that

$$\mathcal{L}_s^* = \bigcup_{\mathbf{k} \in \mathcal{K}_c^*} \{\mathbf{k}+\mathbf{g}\}_{\mathbf{g} \in \mathcal{L}_c^*} \tag{15}$$

holds. This implies that $\mathbf{G} = \mathbf{k} + \mathbf{g}$ is a reciprocal lattice vector of the supercell (dashed vector in Fig. 2) and that the Fourier transform (12) alternatively can be written as

$$G(\mathbf{r}, \mathbf{r}') = \sum_{\mathbf{G}\mathbf{G}' \in \mathcal{L}_s^*} e^{-i\mathbf{G}\mathbf{r}} G(\mathbf{G}, \mathbf{G}') e^{i\mathbf{G}'\mathbf{r}'}. \tag{16}$$

The notation $G(\mathbf{G}, \mathbf{G}')$ indicates a single huge matrix with indices $\mathbf{G}, \mathbf{G}' \in \mathcal{L}_s^*$. However, one has to keep in mind that this matrix is essentially block diagonal. That is, for two reciprocal

lattice vectors $\mathbf{G} = \mathbf{k} + \mathbf{g}$ and $\mathbf{G}' = \mathbf{k}' + \mathbf{g}'$, the matrix reads as

$$G(\mathbf{G},\mathbf{G}') = \delta_{\mathbf{k}\mathbf{k}'} G_{\mathbf{k}}(\mathbf{g},\mathbf{g}'). \qquad (17)$$

Therefore, the two representations (16) and (12) have the same complexity.

In analogy, using inverse arguments for the polarizability, one obtains the two real-space Fourier representations

$$\chi_{\mathbf{k}}(\mathbf{g},\mathbf{g}') = \sum_{\mathbf{r}\mathbf{r}'\in C} e^{i(\mathbf{k}+\mathbf{g})\mathbf{r}} \chi(\mathbf{r},\mathbf{r}') e^{-i(\mathbf{k}+\mathbf{g}')\mathbf{r}'}, \qquad (18)$$

$$\chi(\mathbf{G},\mathbf{G}') = \sum_{\mathbf{R}\mathbf{R}'\in S} e^{i\mathbf{G}\mathbf{R}} \chi(\mathbf{R},\mathbf{R}') e^{-i\mathbf{G}'\mathbf{R}'}. \qquad (19)$$

We summarize the most important result of this section so far. The relations (12) and (16) imply that the Fourier transformation can be evaluated in two different ways. In Eq. (12), the Fourier transformation $G_{\mathbf{k}}(\mathbf{g},\mathbf{g}')$ is a set of $\mathcal{N} \times \mathcal{N} \times \mathcal{N}$ individual matrices "centered" at $\mathbf{k} \in \mathcal{K}_c^*$ with reciprocal lattice vectors of the unit cell $\mathbf{g} \in \mathcal{L}_c^*$. Alternatively, the Green's function (16) can be considered to be a single huge block-diagonal matrix $G(\mathbf{G},\mathbf{G}')$ with matrix indices $\mathbf{G},\mathbf{G}'$ of the reciprocal lattice of the supercell $\mathcal{L}_s^*$. We note that Steinbeck *et al.* used similar strategies, but with one crucial difference: in their work, an auxiliary supercell Green's function is defined without the Bloch phase factors $e^{-i\mathbf{k}(\mathbf{r}-\mathbf{r}')}$. Although elegant, we found no way to extend this prescription to the PAW methodology discussed below. The present strategy is equally efficient, but exploits the translational symmetry relations

$$G(\mathbf{r} - \mathbf{a}, \mathbf{r}') = G(\mathbf{r}, \mathbf{r}' + \mathbf{a}), \qquad (20)$$

$$G(\mathbf{r}, \mathbf{r}') = G^*(\mathbf{r}', \mathbf{r}) \qquad (21)$$

instead.

These relations follow trivially from the definition of the Green's function

$$G(\mathbf{r},\mathbf{r}',i\tau) = \sum_n \psi_n(\mathbf{r})\psi_n^*(\mathbf{r}') e^{-\epsilon_n \tau} \qquad (22)$$

and imply the symmetry of the matrix $G(\mathbf{R},\mathbf{R}')$ illustrated in Fig. 3 with the irreducible stripe $G(\mathbf{r},\mathbf{R}')$ depicted by the thick rectangle. This stripe is obtained from the primitive block $G_{\mathbf{k}}(\mathbf{r},\mathbf{r}')$ using

$$G_{\mathbf{k}}(\mathbf{r},\mathbf{R}' = \mathbf{r}' + \mathbf{a}) = e^{-i\mathbf{k}\mathbf{a}} G_{\mathbf{k}}(\mathbf{r},\mathbf{r}') \qquad (23)$$

with (12) and contains all necessary data in order to determine the remaining matrix elements of the super matrix $G(\mathbf{R},\mathbf{R}')$.

In practice, we exploit these symmetries and evaluate the Fourier transformation of the Green's function in two steps:

$$G(\mathbf{r},\mathbf{k}+\mathbf{g}') = \sum_{\mathbf{g}\in\mathcal{L}_c^*} G_{\mathbf{k}}(\mathbf{g},\mathbf{g}') e^{i(\mathbf{k}+\mathbf{g})\mathbf{r}}, \qquad (24)$$

$$G(\mathbf{r},\mathbf{R}') = \sum_{\mathbf{G}'\in\mathcal{L}_s^*} e^{-i\mathbf{G}'\mathbf{R}'} G(\mathbf{r},\mathbf{G}'). \qquad (25)$$

The first spatial index of the Green's function G is determined by an FFT using the unit cell C, and the second spatial index by an FFT with respect to the supercell S. In the second FFT, $\mathbf{G}'$ is the union of $\mathbf{k} + \mathbf{g}'$ as specified in Eq. (15). Hence, the first spatial index of G is restricted to the unit cell,
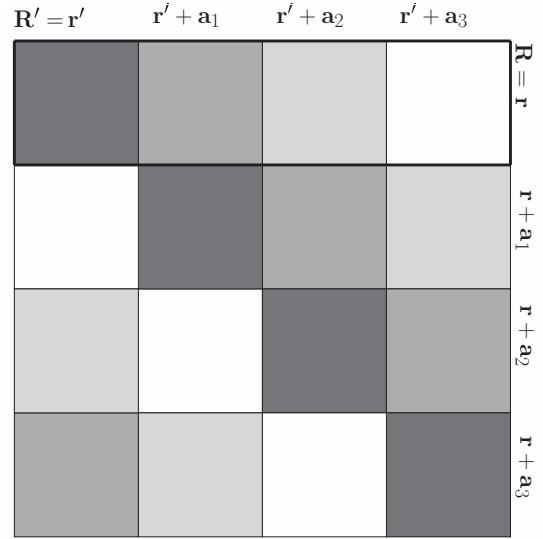

FIG. 3. Symmetry of the Green's function matrix in real space $G(\mathbf{R},\mathbf{R}')$ for a $S = (2 \times 1)C$ supercell with the irreducible stripe $G(\mathbf{r},\mathbf{R}')$ (thick rectangle). Due to Eq. (21), the blocks below the diagonal are complex conjugated.

whereas the second extends over the entire supercell building the irreducible stripe $G(\mathbf{r},\mathbf{R}')$.

Analogously, the FFT of the RPA polarizability from real space to reciprocal space is determined by

$$\chi(\mathbf{r},\mathbf{G}') = \sum_{\mathbf{R}'\in S} \chi(\mathbf{r},\mathbf{R}') e^{i\mathbf{G}'\mathbf{R}'}, \qquad (26)$$

$$\chi_{\mathbf{k}}(\mathbf{g},\mathbf{g}') = \sum_{\mathbf{r}\in C} e^{-i(\mathbf{k}+\mathbf{g})\mathbf{r}} \chi(\mathbf{r},\mathbf{k}+\mathbf{g}'). \qquad (27)$$

Because of $|\mathcal{L}_s^*| = N_k|\mathcal{L}_c^*| = N_k N_b$ (with N_b being the total number of considered basis vectors $\mathbf{g}$) the time complexity for all steps (24)–(27) is of the order

$$\ln\left(N_b^2 N_k\right) N_b^2 N_k \approx \ln(M^2 N_k) M^2 N_k, \qquad (28)$$

i.e., roughly linear in N_k and quadratic in the system size M.

A final remark concerning the first FFT in Fig. 1 is in place here. In principle, the FFT step for the Green's functions from reciprocal to real space can be avoided by evaluating the Green's function directly on the real-space grid. However, this would require considerably more storage for the Green's function and would increase the computational cost since the number of real-space points is at least twice but often up to eight times larger than the number of plane-wave coefficients.

C. Forming $G(i\tau)G(-i\tau)$ in the PAW basis

In analogy to the previous section, here and in the following small bold letters indicate vectors of the unit cell, whereas capital letters represent vectors in the super cell.

In this section, we discuss the contraction of two Green's functions in the space-time domain yielding the independent-particle polarizability [40,41]

$$\chi(\mathbf{r},\mathbf{R}',i\tau) = -G(\mathbf{r},\mathbf{R}',i\tau) G^*(\mathbf{r},\mathbf{R}',-i\tau). \qquad (29)$$

For the PAW basis, this is a rather involved step and requires careful consideration. We start with a short review of the PAW method.

Within the PAW approach, the all-electron orbital ψ_i is represented by the corresponding pseudo-orbital $\tilde{\psi}_i$ via the linear transformation [53,54]

$$|\psi_i\rangle = |\tilde{\psi}_i\rangle + \sum_\mu (|\phi_\mu\rangle - |\tilde{\phi}_\mu\rangle)\langle\tilde{p}_\mu|\tilde{\psi}_i\rangle. \qquad (30)$$

Here, the second term acts only within the augmentation sphere Ω_R enclosing the atoms. The index $\mu = (\mathbf{R}_\mu, n_\mu, l_\mu, m_\mu)$ is an abbreviation for the atomic site $\mathbf{R}_\mu$, the energy quantum number n_μ and angular momentum numbers (l_μ, m_μ) characterizing the solution ϕ_μ of the Schrödinger equation for a reference atom. The pseudocounterparts $\tilde{\phi}_\mu$ are smooth functions coinciding with ϕ_μ outside Ω_R. They are dual to the projectors $\tilde{p}_\mu$ within Ω_R:

$$\langle\tilde{p}_\mu|\tilde{\phi}_\nu\rangle = \delta_{\mu\nu}. \qquad (31)$$

For further information about the chosen projectors $\tilde{p}_\mu$ and pseudopartial waves $\tilde{\phi}_\mu$, we refer the reader to the literature [53,54].

Representing the all-electron orbitals ψ_i by pseudo-orbitals $\tilde{\psi}_i$ using Eq. (30), additional contributions to χ, defined in Eq. (3), appear. These contributions stem from the evaluation of the all-electron matrix elements [54,55]

$$\langle\psi_i|e^{i(\mathbf{k}+\mathbf{g})\mathbf{r}}|\psi_a\rangle$$
$$= \langle\tilde{\psi}_i|e^{i(\mathbf{k}+\mathbf{g})\mathbf{r}}|\tilde{\psi}_a\rangle + \sum_{\mathbf{r}\in C} e^{i(\mathbf{k}+\mathbf{g})\mathbf{r}} \sum_{\mu\nu}\langle\tilde{\psi}_i|\tilde{p}_\mu\rangle$$
$$\times Q_{\mu\nu}(\mathbf{r})\langle\tilde{p}_\mu|\tilde{\psi}_a\rangle. \qquad (32)$$

Here, the auxiliary function $Q_{\mu\nu}$,

$$Q_{\mu\nu}(\mathbf{r}) = \phi_\mu^*(\mathbf{r})\phi_\nu(\mathbf{r}) - \tilde{\phi}_\mu^*(\mathbf{r})\tilde{\phi}_\nu(\mathbf{r}), \qquad (33)$$

describes the difference between the charge density of the pseudopartial and all-electron partial waves. Typically, this function is oscillatory in the augmentation sphere Ω_R, so that in practice further approximations to $Q_{\mu\nu}$ are applied. In the present code, the function is expanded in an orthogonal set of functions, and the rapid spatial oscillations are neglected beyond a certain plane-wave energy cutoff [54,56].

Using Eqs. (32) and (3) and Fourier transforming the RPA response function to real space and imaginary time $i\tau$, the resulting expression for $\chi(\mathbf{r},\mathbf{R}',i\tau)$ contains four terms

$$\chi(\mathbf{r},\mathbf{R}',i\tau) = \sum_{j=1}^4 \chi^{(j)}(\mathbf{r},\mathbf{R}',i\tau). \qquad (34)$$

Each contribution $\chi^{(j)}$ is characterized as follows: $\chi^{(1)}$ contains a summation of pseudoterms only

$$\chi^{(1)}(\mathbf{r},\mathbf{R}',i\tau) \propto \xi_{ia}(i\tau)\tilde{\psi}_i(\mathbf{r})\tilde{\psi}_i^*(\mathbf{R}')\tilde{\psi}_a^*(\mathbf{r})\tilde{\psi}_a(\mathbf{R}') \qquad (35)$$

and is represented on a plane-wave grid. The second $\chi^{(2)}$ and third contribution $\chi^{(3)}$ contain terms from one augmentation sphere

$$\chi^{(2)}(\mathbf{r},\mathbf{R}',i\tau) \propto \xi_{ia}(i\tau)\tilde{\psi}_i(\mathbf{r})\tilde{\psi}_a^*(\mathbf{r})$$
$$\times \sum_{\alpha\beta}\langle\tilde{\psi}_i|\tilde{p}_\alpha\rangle Q_{\alpha\beta}(\mathbf{R}')\langle\tilde{p}_\beta|\tilde{\psi}_a\rangle, \qquad (36)$$

$$\chi^{(3)}(\mathbf{r},\mathbf{R}',i\tau) \propto \xi_{ia}(i\tau)\tilde{\psi}_i^*(\mathbf{R}')\tilde{\psi}_a(\mathbf{R}')$$
$$\times \sum_{\mu\nu}\langle\tilde{\psi}_a|\tilde{p}_\mu\rangle Q_{\mu\nu}(\mathbf{r})\langle\tilde{p}_\nu|\tilde{\psi}_i\rangle. \qquad (37)$$

The fourth term contains only augmentation terms

$$\chi^{(4)}(\mathbf{r},\mathbf{R}',i\tau) \propto \xi_{ia} \sum_{\mu\nu}\langle\tilde{\psi}_a|\tilde{p}_\mu\rangle Q_{\mu\nu}(\mathbf{r})\langle\tilde{p}_\nu|\tilde{\psi}_i\rangle$$
$$\times \sum_{\alpha\beta}\langle\tilde{\psi}_i|\tilde{p}_\alpha\rangle Q_{\alpha\beta}(\mathbf{R}')\langle\tilde{p}_\beta|\tilde{\psi}_a\rangle. \qquad (38)$$

All terms need to be accounted for when computing the RPA polarizability from Green's functions using the contraction formula (29). For this purpose, we define the following Green's functions:

$$G_{\mathbf{k}}^{(1)}(\mathbf{g},\mathbf{G}',i\tau) = \sum_n \langle\tilde{\psi}_{n\mathbf{k}}|\mathbf{g}\rangle\langle\mathbf{G}'|\tilde{\psi}_{n\mathbf{k}}\rangle e^{-\epsilon_{n\mathbf{k}}\tau}, \qquad (39)$$

$$G_{\mathbf{k}}^{(2)}(\mu,\mathbf{G}',i\tau) = \sum_n \langle\tilde{\psi}_{n\mathbf{k}}|\tilde{p}_\mu\rangle\langle\mathbf{G}'|\tilde{\psi}_{n\mathbf{k}}\rangle e^{-\epsilon_{n\mathbf{k}}\tau}, \qquad (40)$$

$$G_{\mathbf{k}}^{(3)}(\mathbf{g},\alpha,i\tau) = \sum_n \langle\tilde{\psi}_{n\mathbf{k}}|\mathbf{g}\rangle\langle\tilde{p}_\alpha|\tilde{\psi}_{n\mathbf{k}}\rangle e^{-\epsilon_{n\mathbf{k}}\tau}, \qquad (41)$$

$$G_{\mathbf{k}}^{(4)}(\mu,\alpha,i\tau) = \sum_n \langle\tilde{\psi}_{n\mathbf{k}}|\tilde{p}_\mu\rangle\langle\tilde{p}_\alpha|\tilde{\psi}_{n\mathbf{k}}\rangle e^{-\epsilon_{n\mathbf{k}}\tau}, \qquad (42)$$

where the notation

$$\langle\tilde{\psi}_{n\mathbf{k}}|\mathbf{g}\rangle = \sum_{\mathbf{r}\in C} \tilde{\psi}_{n\mathbf{k}}^*(\mathbf{r})e^{i(\mathbf{k}+\mathbf{g})\mathbf{r}}, \qquad (43)$$

$$\langle\tilde{\psi}_{n\mathbf{k}}|\mathbf{G}'\rangle = \sum_{\mathbf{R}'\in S} \tilde{\psi}_{n\mathbf{k}}^*(\mathbf{R}')e^{i\mathbf{G}'\mathbf{R}'} \qquad (44)$$

was used, the Fermi energy was set to $\epsilon_F = 0$ and $\mathbf{G}' = \mathbf{k} + \mathbf{g}'$ is assumed for Eqs. (39)–(41). For each function $G^{(j)}$ two representatives $\underline{G}^{(j)}, \overline{G}^{(j)}$, for occupied and unoccupied states, are stored. Occupied Green's functions ($\epsilon_i < 0$) are thereby evaluated on the negative, unoccupied functions ($\epsilon_i > 0$) on the positive time axis τ only. In this way, the resulting Green's functions $G^{(j)}$ are linear combinations of decaying exponentials and therefore bounded in time.

The computational cost for each term $G^{(j)}$ is

$$N_\omega N_k N_b^3 \approx N_\omega N_k M^3, \qquad (45)$$

where N_ω is the number of imaginary grid points. Using the FFTs (24) and (25) from the previous section, the real-space Green's functions are contracted as follows:

$$\chi(\mathbf{r},\mathbf{R}',i\tau) = \underline{G}^{(1)}(\mathbf{r},\mathbf{R}',i\tau)\overline{G}^{*(1)}(\mathbf{r},\mathbf{R}',-i\tau)$$
$$+ \sum_{\mu\nu}\underline{G}^{(2)}(\mu,\mathbf{R}',i\tau)\overline{G}^{*(2)}(\nu,\mathbf{R}',-i\tau)Q_{\mu\nu}(\mathbf{r})$$
$$+ \sum_{\alpha\beta}\underline{G}^{(3)}(\mathbf{r},\alpha,i\tau)\overline{G}^{*(3)}(\mathbf{r},\beta,-i\tau)Q_{\alpha\beta}(\mathbf{R}')$$
$$+ \sum_{\mu\nu\alpha\beta}\underline{G}^{(4)}(\mu,\alpha,i\tau)\overline{G}^{*(4)}(\nu,\beta,-i\tau)$$
$$\times Q_{\mu\nu}(\mathbf{r})Q_{\alpha\beta}(\mathbf{R}'). \qquad (46)$$

Here, the atom positions $\mathbf{R}_\mu, \mathbf{R}_\nu$ are restricted to the unit cell C, while $\mathbf{R}_\alpha, \mathbf{R}_\beta$ take values within the supercell S (cf. Sec. II B)

[41]. From $\chi(\mathbf{r},\mathbf{R}',i\tau)$, $\chi_{\mathbf{k}}(\mathbf{g},\mathbf{g}')$ at individual k points is finally determined using Eqs. (26) and (27), and the correlation energy in the random phase approximation is then determined in the usual manner at each k point.

Considering the computational time for each step (46), (45), (28), and (8) for the evaluation of E^{RPA} shows that the present algorithm determines the RPA energy with a computational cost of $\approx N_k N_b^3$. This reduces the time complexity by a factor $\approx N_k N_b$ compared to previous implementations.

D. Symmetry

The present code allows us to use symmetry partially. For instance, the density functional theory calculations are performed using only the irreducible wedge of the Brillouin zone, and furthermore the RPA correlation energy is only calculated at the irreducible k points $\mathbf{k}$ using $\chi_{\mathbf{k}}(\mathbf{g},\mathbf{g}')$ [compare Eq. (27)]. The Green's function $G_{\mathbf{k}}(\mathbf{g},\mathbf{g}')$ could be also constructed in the irreducible wedge, however, presently we first use symmetry to construct the orbitals at the all k points and then construct the Green's function for all k points in the full Brillouin zone.

Currently, we disregard any symmetry, whenever a supercell index $\mathbf{G}$ or $\mathbf{R}$ is involved. This implies that all quadratically scaling steps fail to benefit from symmetry, whereas the cubically scaling steps [except the construction of $G_{\mathbf{k}}(\mathbf{g},\mathbf{g}')$] exploit symmetry. This seems to be a reasonable compromise between the implementation effort and the compute cost.

III. TECHNICAL DETAILS

In this work, all calculations were performed using the Vienna *ab initio* simulation package (VASP) using the projector augmented wave method of Blöchl in the implementation of Kresse and Joubert [53,54]. The Si potential was constructed to conserve the scattering properties of the atoms well up to about 15 Ry above the vacuum level. This was achieved by using additional projectors above the vacuum level. Core radii of 1.90 a.u. were used. Specifically, the Si_GW potential released with VASP.5.2 was employed.

All plane waves with the kinetic energy E_{cut} lower then 250 eV are used in the DFT calculations, and the DFT calculations are performed using the Perdew-Burke-Ernzerhof (PBE) functional [57]. The EXX + RPA@PBE calculations are performed at the same plane-wave cutoff. When summations over unoccupied Kohn-Sham states are required (virtual orbitals), all orbitals spanned by the basis set are determined by exact diagonalization of the Kohn-Sham Hamiltonian. The correlation energy in the random phase approximation E^{RPA} is then calculated as discussed in the previous section.

The response function itself is also expanded in a plane-wave basis set. The plane-wave cutoff for this basis set is set to 120–166 eV (smaller than the basis set for the orbitals), and the correlation energy is extrapolated to the infinite basis set limit assuming that the basis set error falls off like the inverse of the number of plane waves included in the basis set for the response function [5]. In the VASP code, this requires a single calculation, as the response function is truncated at different cutoffs after calculation at the largest basis set of 166 eV. The extrapolation is performed automatically by

the code, requiring a minimum of extra computational time. The structures used for the calculations were determined by relaxing all internal degrees of freedom at the PBE level (keeping the cell shape and volume fixed). In the subsequent RPA calculations, the PBE structures were used since forces and the stress tensor are presently not available. Similar strategies are also routinely adopted in diffusion Monte Carlo simulations and most quantum chemistry, e.g., coupled cluster, calculations.

IV. RESULTS

A. Bulk properties

With the present PAW potentials, the volume per atom is 20.46 Å^3 and 15.35 Å^3 for cubic diamond and β-Sn for PBE. As a first test, we calculated the volume per atom for the RPA for these two phases. Using $6 \times 6 \times 6$ k points and $10 \times 10 \times 10$ k points for diamond and β-Sn, respectively, the predicted atomic volumes are 20.0 and 15.25 Å^3, slightly smaller than the PBE volumes. Per atom, the RPA energy difference between the two phases is 380 meV. A similar energy difference of 390 meV using the same PAW potentials was also calculated by Xiao *et al.* [11].

This is 100 meV larger than the energy difference predicted by the PBE functional (280 meV). Using diffusion Monte Carlo (DMC), Batista *et al.*, Alfè *et al.*, and Henning *et al.* predicted values of 480 ± 50 meV [58], 475 ± 10 meV [59], and 424 ± 20 meV [60], respectively (the latter two values are including core polarization contributions). In this case, the DMC does not seem to be suitable to gauge the quality of the RPA since the transition pressure from diamond to the β-Sn phase predicted from the DMC data is about 16.5 GPa [58] and 14.0 ± 1.0 GPa [60], respectively, which is larger than the experimental estimates of 10.3–12.5 GPa [59]. The energy difference predicted by the RPA (380 meV), however, corresponds to a transition pressure of about 13.5 GPa in reasonable agreement with the experimental estimates. The origin of the error of the DMC is not known, but we believe it could be related to the fixed-node approximation, or insufficient convergence of the sampling of the Brillouin zone for the metallic β-Sn phase.

Including the $2s$ and $2p$ electrons in the valence for the RPA calculations has a negligible effect on the predicted volumes [10]. However, it still lowers the energy difference between the two phases to 340 meV. A similar reduction from core polarization was also predicted in DMC calculations [59]. This lowers the predicted transition pressure to 12 GPa, now in excellent agreement with the experimental estimates. Overall, these results support the quality of the RPA predictions. For a more detailed discussion of RPA results, for instance inclusion of zero-point vibration effects, we refer to Xiao *et al.* [11].

B. Time complexity for large supercells

The results for the Si self-interstitials and Si vacancies will be discussed in the next section. Here, we briefly elaborate on the required computation time. The present calculations were performed for 64, 128, and 216 atom supercells (and 256 for the vacancy). The RPA corrections were determined for various k-point grids starting with the Γ point. For the smallest cell, we
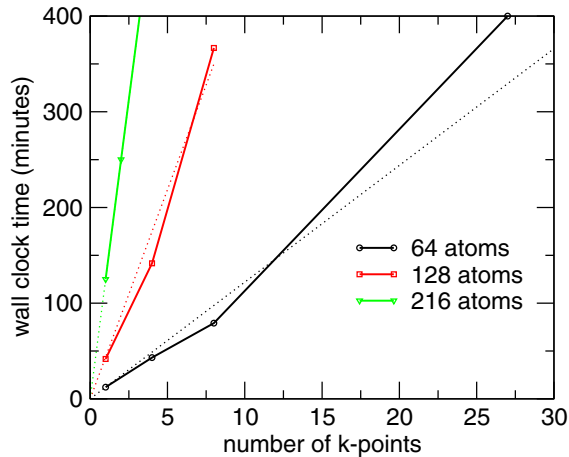
FIG. 4. (Color online) Computational time for 64, 128, and 216 atoms as a function of the number of k points (in the full Brillouin zone). The total (wall clock) time is shown for 64, 128, and 224 cores. The computational demand increases linearly in the number of k points and cubically in the number of atoms. The deviation from linearity is related to the need to double the number of cores for $3 \times 3 \times 3$ k points (64 atoms) and $2 \times 2 \times 2$ k points (128 atoms), and the nonperfect scaling with the number of cores. The corresponding reported compute time has been doubled.

could perform RPA calculations for up to $3 \times 3 \times 3$ k points in less than 4 h on 128 cores, a very modest computational effort. Calculations with more k points are difficult since the memory requirements would force us to increase the number of cores, but the parallel efficiency of the present code version is not yet very good, making such calculations rather inefficient. The loss of efficiency is already witnessed for $3 \times 3 \times 3$ k points, where we had to increase the number of cores from 64 to 128, gaining only little speedup from the additional 64 cores (compare Fig. 4). This is the reason why the reported computation time for 64 atoms and $3 \times 3 \times 3$ k points (scaled back to 64 nodes) deviates from the straight-line behavior. For 128 atoms we performed Γ-only calculations and calculations using $2 \times 2 \times 2$ k points. Again, calculations using $2 \times 2 \times 2$ k points required an increase in the number of cores, here from 128 to about 200. A k-point sampling with four k points was also realized by using only every second k point of the $2 \times 2 \times 2$ grid, corresponding to an fcc subgrid of the full simple cubic grid. For 216 atoms, the calculations were performed with a single k point and two and four k points. The second k point corresponds to the coordinates $(1/4, 1/4, 1/4)$ $2\pi/a$ or a bcc subgrid of a $2 \times 2 \times 2$ mesh.

In order to investigate the scaling with system size in more detail, we performed RPA calcuations for 54, 128, and 250 bcc unit cells using the Γ point (see Table I). The timings reported in Table I and Fig. 4 clearly confirm that the present code scales linearly in the number of k points, and roughly cubically with the number of atoms as discussed at the end of Sec. II C.

A few final comments are in place here. First, the reported timings were obtained using a complex code version. At the Γ point, however, the response function is real valued, which allows us to reduce the computational time by a factor 2 compared to the reported values. The corresponding

TABLE I. Timings in minutes for an RPA calculation for different bulk Si bcc cells. The calculations are done for the Γ point only and the number of cores is increased with system size. Since one of the computational steps scales only quadratically with system size, the total scaling is better than cubic.

Atoms	Cores	Time	Time$\times$cores/atoms^3 $\times 10^3$
54	32	14.3	2.91
128	64	83.2	2.54
250	128	299.9	2.45

calculations take 6 min for 64 atoms on 64 cores, or about 1 h for 216 atoms on 224 cores. The scaling is very close to the expected scaling. We can also compare the computational time to our previous code version that scales quadratically with the number of k points and with the fourth power of the number of atoms. For 64 atoms and the real Γ-point version, the old version required a reasonable 30 min (only a factor 5 slower than the new version), however, for four k points the calculations are already a factor 10 slower, and for $3 \times 3 \times 3$ k points we expect the factor to be around 100. Considering common runtime constraints on supercomputers, this would make the calculations almost impossible using the previous RPA implementation [5].

C. Interstitial and vacancy

1. Considered structures and k-points sampling

We start with a brief discussion of the various self-interstitials. The energetically most stable self-interstitial is the so-called dumbbell configuration (X), in which two Si atoms reside at the position originally occupied by a single Si atom. The "dimer" is placed symmetrically in this position and oriented parallel to the [110] direction. The second most favorable position is the hexagonal hollow (H), where the Si interstitial is coordinated to six Si atoms forming a hexagonal ring. In PBE, this position is unstable, and the central Si atom tends to move slightly away from the central position in a direction orthogonal to the hexagonal ring [61]. As for instance done by Rinke *et al.*, we denote this lower-symmetry sixfold-coordinated position as C_{3v} (corresponding to the symmetry of this configuration) [62]. Somewhat higher in energy than the other interstitial sites is the tetragonal site (T), in which the additional Si atom is coordinated to four nearest Si neighbors, so that the local coordination of the interstitial is identical to the other Si atoms. This position is unique insofar that the highest occupied orbital is threefold degenerate (t_2 symmetry) but only occupied by two electrons. This would suggest that the position is susceptible to a Jahn-Teller distortion, but at least in PBE and for 64 atoms, a calculation of all vibrational modes does not show any instabilities. Likewise, the vacancy (V) is characterized by a threefold-degenerate t_2 highest orbital that is also occupied by two electrons. This configuration is known to undergo a Jahn-Teller distortion to a D_{2d} symmetry with slow supercell convergence [63]. In PBE, we observe the distortion from the 216-atom cell on, with the distortion fully developed only for a 256-atom cell; e.g., the magnitude of the structural distortion is about 25% smaller in the 216-atom cell than in the 256-atom cell. For the smaller cells, the distortion only

TABLE II. The second, third, and fourth columns report the difference between RPA and PBE formation energies for different defect configurations, k points and supercells, with the k-point set indicated in the first row (all values in eV). The second row in each set reports the k-point convergence of the PBE formation energies. The columns PBE and RPA report the final converged formation energies. The RPA value was calculated by adding the most accurate corrections to the k-point converged PBE values. The range separated rsRPA values are from Ref. [65], and the values for HSE + vdW are from Ref. [64].

16 atoms	2^3	3^3	4^3	PBE	RPA	
X(PBE)	2.525	3.481	3.541	3.561		
X	0.824	0.706	0.711	3.561	4.27	
C$_{3v}$	0.855	0.800	0.745	3.644	4.39	
H	0.830	0.750	0.707	3.740	4.45	
T	0.930	0.882	0.868	3.659	4.53	
V	0.426	0.444	0.446	3.023	3.47	
X→H	0.862	0.809	0.760	3.783	4.54	
64 atom	Γ	2^3	3^3	PBE	RPA	rsRPA
X(PBE)	2.440	3.616	3.611	3.614		
X	0.818	0.659	0.654	3.614	4.27	4.50
C$_{3v}$	0.849	0.788	0.745	3.651	4.40	
H	0.820	0.753	0.708	3.658	4.37	4.65
T	1.025	1.080	1.046	3.790	4.84	
VJT	0.851	0.813	0.781	3.642	4.42	4.24
X→H	0.789	0.770	0.698	3.924	4.62	4.99
128 atom	Γ	4	2^3	PBE	RPA	
X(PBE)	2.662	3.603	3.571	3.610		
X	0.814	0.670	0.683	3.610	4.29	
C$_{3v}$	0.843	0.839	0.817	3.647	4.46	
H	0.832	0.775	0.755	3.654	4.41	
T	1.153	1.078	1.112	3.766	4.88	
VJT	0.855	0.795	0.829	3.636	4.47	
216 atom	Γ	2	4	PBE	RPA	HSE +vdW
X(PBE)	3.256	3.341	3.571	3.566		
X	0.724	0.710	0.632	3.566	4.20	4.41
C$_{3v}$	0.820	0.812	0.743	3.619	4.36	4.40
H	0.789	0.779	0.707	3.626	4.33	
T	1.105	1.144	1.139	3.791	4.93	4.51
VJT	0.789	0.755	0.742	3.646	4.39	4.38
256 atom	Γ	2		PBE	RPA	
VJT(PBE)	3.272	3.518		3.589		
VJT	0.839	0.745		3.589	4.33	

occurs if the k-point mesh is chosen artificially coarse (e.g., $2 \times 2 \times 2$ for 64 atoms), and we have used such k-point sets to prepare the symmetry-reduced Jahn-Teller distorted vacancy configuration (VJT). The energy difference to the undistorted configuration is, however, small and only of the order of 20 meV and can be safely disregarded for the present purpose.

The DFT calculations were carefully converged. In agreement with other studies, we found that $4 \times 4 \times 4$ k points are usually sufficient for 64-atom cells, and $2 \times 2 \times 2$ k points for 216-atom cells [63,64]. The only exception is the metallic T configuration, which in our calculations only converged to meV accuracy using slightly more k points. The final PBE values reported in Table II were obtained using $8 \times 8 \times 8$,

$6 \times 6 \times 6$, $4 \times 4 \times 4$, and $3 \times 3 \times 3$ k points for 16, 64, 128, and 216 atoms. For the Si vacancy, also a 256-atom cell with $3 \times 3 \times 3$ k points was used. With these settings, the values are converged to within a few meV. Except for a constant offset, the present PBE values agree well with the values reported by Gao *et al.* [64]. It is gratifying that two very different codes can obtain some 10-meV agreement for tiny relative energy differences, when the setups are carefully converged.

2. Energetics of point defects

The results for Si self-interstitials and Si vacancies are summarized in Table II. The RPA energies were evaluated using 16 frequency points. For 64 atoms, increasing the number of frequency points from 16 to 20 changed the results by less than 0.5 meV supporting the previous claim that few μeV accuracy per atom can be attained (the changes are largest for the defects with very small or even vanishing Kohn-Sham one-electron gaps). Here, we adopted the strategy to evaluate the difference between RPA + EXX and PBE at various k-point sets. This strategy seems to work quite well: even though the PBE energies are wrong by more than 1.2 eV using the Γ point only [see lines marked X(PBE)], the error in the difference between RPA + EXX and PBE is at most 150 meV at the Γ point for 64 atoms. First useful corrections to DFT can hence be obtained already with a rather coarse sampling. With $2 \times 2 \times 2$ k points, the errors in the RPA correction are below 50 meV, which is most likely acceptable for many purposes. For 128 atoms, the difference between four k points (the fcc grid) and eight k points is a rather modest 20 meV. As a general rule of thumb, it seems that the k-point errors in the RPA corrections are about $\frac{1}{3}$ of the k-point errors of the PBE energies. This also suggests that four and two k points will yield only errors of about 10–20 meV for the calculation of the RPA correction for the 216- and 256-atom cells, respectively.

Considering the Γ-point only, the errors in the DFT energies and the RPA corrections are 300 and 100 meV, respectively, for the largest cells (216 and 256 atoms). This confirms the observation of many previous studies that calculations at the Γ point should be considered with caution. Furthermore, we note that the convergence with the number of atoms of both the DFT energies and the corrections is not monotonic but shows some residual fluctuations. This might be expected since the cell shape, simple cubic for 64 and 216 atoms, but fcc for 128 atoms, influences the electronic dispersion, the long-range electrostatic, as well as elastic interactions between the defects [63,66]. For the present case, the k-point converged RPA formation energies vary by at most 100 meV between different super cells.

We start with a comparison with the most accurate theoretical values presently available, DMC data. Our results yield consistently lower formation energies than all DMC calculations, although the agreement with the latest DMC data is overall very good, in particular, for relative energies. Parker *et al.* predicted values of 4.4(1), 5.1(1), and 4.7(1) for X, T, and H using DMC [67], compared to our values of 4.20, 4.93, and 4.33 (largest supercell). We tend to believe that the residual underestimation by 200 meV is an error of the RPA since the DMC values are so consistently higher in energy [58,67,68]. However, one should also keep in mind that most

DMC calculations were performed with fairly small 16-atom supercells [58] with extrapolation to the dilute limit based on DFT energies. Likewise, the k-point sampling in the DMC calculations was always limited to a single k point, which might affect the predicted energies. In most DMC calculations, however, many-electron k-point errors due to the discretization of the momentum transfer between two k points are estimated using the structure factor method, a method we could but have not applied in our RPA calculations [67,69]. This implies that the k-point errors that we observe in the RPA are not transferable to well-extrapolated DMC calculations, where many electron k-point errors are expected to be much smaller.

The present formation energies are also very well within the range of experimental values and, furthermore, agree reasonably well with the HSE calculations of Gao *et al.* [64], and to a lesser extent with the HSE + vdW calculations by the same authors. Specifically, the most stable structure is the dumbbell configuration X, followed by the interstitial in the hexagonal hole H, which is about 100 meV higher in energy, in excellent agreement with HSE calculations. The main discrepancy to the results of Gao is our instability of the tetragonal site [64]. In our calculations, this site is 600 meV above the dumbbell configuration X (in agreement with DMC data). In HSE, the difference is only 300 meV, and in HSE + vdW it is just 100 meV. In vdW-DFT this configuration is lowered compared to HSE by an increase of the polarization at the four nearest-neighbor sites in the HSE + vdW calculations. In agreement with this observation, our negative correlation energy is largest for this metallic configuration, almost 2 eV lower than for the other interstitial sites. However, the unfavorable EXX energy of this configuration more than makes up for this increase in the correlation energy. The origin for the unfavorable EXX energy is the "metal-like" behavior of this specific configuration with three degenerate partially occupied p orbitals at the Fermi level: As for any metallic configuration, exact exchange penalizes this configuration, here by more than 2 eV. This is also the reason why this configuration is less favorable in hybrid functionals. We believe that the present seamless approach should give a better description than an introduction of vdW corrections on top of a hybrid functional with an *ad hoc* mixture between exact exchange and semilocal exchange. After all, vdW-DFT is derived from the RPA correlation energy expression considering the interaction between two coupled quantum harmonic oscillators [22]. However, one also needs to concede that the accuracy of the RPA for configurations with symmetry-degenerate states at the Fermi level is certainly not yet fully established and this issue might require further studies. Before continuing, we finally note that the RPA does predict the hexagonal hole to be lower in energy than the symmetry-broken C_{3v} configuration. This is consistently observed for all supercell sizes. In this case, RPA clearly does not favor a symmetry-broken solution, whereas PBE does.

3. *Diffusion barrier of interstitial*

The final quantity we consider is the diffusion barrier of the interstitial Si atom. In all recent publications, including range-separated RPA and vdW corrected HSE, it was agreed that the lowest activation barrier for diffusion is encountered for the

diffusion of one atom from the dumbbell configuration X to the hexagonal hole H [64,65]. We first tested this conjecture by performing finite-temperature molecular dynamics at 800 K for the 64-atom cell, the PBE functional, and a $3 \times 3 \times 3$ k-point mesh. Indeed, Si diffuses fairly rapidly with all diffusion events occurring from the dumbbell configuration X to the hollow site H, followed by a rapid jump from H to another site X'. In the RPA calculations, the estimated activation enthalpy for interstitial diffusion is 4.62 eV (64-atom cell), in very good agreement with estimates of 4.69 eV [70], but smaller than the estimates of Bracht *et al.* (4.95±0.03 eV) [71]. The diffusion barrier from X to H is calculated to be 350 meV, only slightly larger than the recent value predicted from HSE + vdW (290 meV) [64]. Both values are in reasonable, but certainly not great, agreement with the best experimental estimates of 200 meV measured at cryogenic temperatures ($-273\,°C$ to $-150\,°C$) [72]. The remaining difference between RPA and HSE + vdW could be related to the fact that we have used PBE geometries throughout this work, whereas Gao *et al.* performed the calculations consistently using geometries determined by HSE + vdW.

Our present estimate for the diffusion barrier differs from the value of 490 meV obtained using range-separated RPA (rsRPA) by Bruneval [65]. Furthermore, whereas the vacancy formation energy of 4.33 eV is identical to rsRPA, our interstitial formation energies are about 200–300 meV lower than those predicted using rsRPA [65]. Since the technical parameters of the calculations of Bruneval are similar to our setups, this is either a consequence of different pseudopotentials or range separation. Although range separation is an approach that allows us to reduce the number of occupied orbitals with little impact on accuracy, the results, to some extent, always depend on the range-separation parameter, and the optimal choice varies between systems with small lattice constants (large Fermi vector) and systems with large lattice constants (small Fermi vector). Also, range separation spoils the basis-set extrapolation: for standard RPA the extrapolation with the basis-set size of the response function strictly follows a one over basis-set size behavior for all systems we have yet considered. This is not the case, when range separation is used, so that residual errors are difficult to control and estimate. In general, we hence prefer, whenever computable, the standard RPA to an approximate method.

4. *Small unit cells*

Finally, we would like to comment on the smallest 16-atom unit cell since most high-level DMC calculations are performed for such a small unit cell. Except for the tetragonal site and vacancy, the results are in reasonable agreement with the larger unit cells, both on the level of the PBE, as well as, on the level of the RPA. Furthermore, the calculated energy correction PBE-RPA are accurate to about 50 meV, except again for the vacancy and tetragonal site. We recall that these are the two configurations resulting in partially filled states. Obviously, aggregation of such defects reduces their formation energy. This effect is most pronounced and only relevant for the vacancy, which is predicted to be much more stable in the 16-atom unit cell than in the larger unit cells. In fact, our results imply that, configuration entropy disregarded,

vacancies should cluster. This is in agreement with Ref. [73], where diffusion of vacancies in Si has been investigated.

V. DISCUSSION AND CONCLUSIONS

In this work, we have discussed a cubic scaling algorithm for the calculation of the RPA correlation energy and have shown practical applications of the algorithm to supercells containing up to 256 atoms.

The main strategy of the cubic scaling algorithm is to determine the Green's function for positive and negative imaginary time and, concomitantly, occupied and unoccupied states. This step scales like $N_{\text{orbitals}} \times N_b \times N_b$, where N_b specifies the basis-set size for the orbitals [see Eq. (45)].

The independent-particle polarizability is then trivially given by the pointwise contraction in real space of these two Green's functions at any considered time point [cf. Eq. (29)]. The contraction is formally only a step scaling like $N_{\text{real}} \times N_{\text{real}}$, where N_{real} is the number of grid points in real space. In practice, this step is fairly involved in the PAW method, so that the computational time of this step is often similar to the calculation of the Green's functions itself [see Eq. (46) in Sec. II C].

The final step is the Fourier transformation from imaginary time to imaginary frequency. This step is discussed in more detail in another publication also elaborating on the issue of optimal time and frequency grids and their duality in detail. We, however, stress here that an accuracy of few μeV/atom can be attained using about 16 imaginary time and frequency points. After the Fourier transformation to imaginary frequency, the calculations proceed in the same manner as standard RPA calculations, by diagonalization of the polarizability using the plasmon formula for the correlation energy [cf. Eq. (1)].

As demonstrated here, calculations for 64 Si atoms and $3 \times 3 \times 3\, k$ points can be performed in about 5 h on 128 cores. About the same time is required for 216 Si atoms and 2 k points. Because the polarizability is real valued at the Γ point, the Γ-point only calculations are much cheaper, requiring about 6 min for 64 atoms on 64 cores, or 1 h for 216 atoms on 224 cores. To put the effort for all the RPA calculations into perspective: the computation time for calculating all occupied and unoccupied orbitals spanned by the basis set using an efficient parallel SCALAPACK routine, a prerequisite for RPA calculations, requires about one third

to one half of the computational time of the final RPA step. We hope that this high efficiency makes RPA calculations sufficiently cheap, to perform them routinely *a posteriori* for any system of interest.

The main physical objective of this work was a study of the Si interstitial and Si monovacancy energies at the level of the RPA. The most stable interstitial defect is the dumbbell configuration with a formation energy of 4.20 eV. The activation energy for diffusion from the dumbbell configuration to the hollow site is predicted to be 350 meV. These values are in reasonable agreement with very recent HSE calculations including semiempirical van der Waals corrections (dumbbell energy 4.41 eV and migration barrier 290 meV, respectively). The vacancy formation energy is calculated to be 4.38 eV, also in excellent agreement with the HSE + vdW calculations (4.41 eV). We, however, observe that metallic configurations such as the tetragonal interstitial site are significantly higher in energy than predicted with HSE and HSE + vdW, and generally the energy landscape is not as "washed" out and featureless as in the HSE + vdW prescription. All in all, our results are closer to the straight HSE calculations than the HSE + vdW results, except for the diffusion barrier agreeing well with the HSE + vdW results.

Comparison of the present values with, in principle, highly accurate DMC values is also very gratifying. In general, all predicted interstitial energies are roughly 0.2 eV lower than in DMC. The origin of this small shift might be related to cell-size issues in the DMC or an error of the RPA. Finally, we have reported that the RPA yields a very good prediction for the transition pressure between diamond Si and β-Si of about 12 GPa (when $2s$ and $2p$ electrons are included in the valence). Compared to experiment (10–12 GPa), this is slightly better than the best DMC estimates of about 14 GPa. In general, this work again confirms that the RPA is a promising and quite accurate method to estimate correlation energies. With the present cubically scaling algorithm, defect calculations and the calculation of adsorption energies on surfaces should become a routine task.

ACKNOWLEDGMENTS

[1] D. C. Langreth and J. P. Perdew, Phys. Rev. B **15**, 2884 (1977).

[2] F. Furche, Phys. Rev. B **64**, 195120 (2001).

[3] T. Miyake, F. Aryasetiawan, T. Kotani, M. van Schilfgaarde, M. Usuda, and K. Terakura, Phys. Rev. B **66**, 245103 (2002).

[4] A. Marini, P. García-González, and A. Rubio, Phys. Rev. Lett. **96**, 136404 (2006).

[5] J. Harl and G. Kresse, Phys. Rev. B **77**, 045136 (2008).

[6] F. Furche, J. Chem. Phys. **129**, 114105 (2008).

[7] H. Eshuis, J. Yarkony, and F. Furche, J. Chem. Phys. **132**, 234114 (2010).

[8] H. Eshuis and F. Furche, J. Phys. Chem. Lett. **2**, 983 (2011).

[9] J. Harl and G. Kresse, Phys. Rev. Lett. **103**, 056401 (2009).

[10] J. Harl, L. Schimka, and G. Kresse, Phys. Rev. B **81**, 115126 (2010).

[11] B. Xiao, J. Sun, A. Ruzsinszky, J. Feng, and J. P. Perdew, Phys. Rev. B **86**, 094109 (2012).

[12] T. Olsen and K. S. Thygesen, Phys. Rev. B **87**, 075111 (2013).

[13] L. Schimka, R. Gaudoin, J. Klimeš, M. Marsman, and G. Kresse, Phys. Rev. B **87**, 214102 (2013).

[14] S. Lebègue, J. Harl, T. Gould, J. G. Ángyán, G. Kresse, and J. F. Dobson, Phys. Rev. Lett. **105**, 196401 (2010).

[15] T. Olsen, J. Yan, J. J. Mortensen, and K. S. Thygesen, Phys. Rev. Lett. **107**, 156401 (2011).

[16] F. Mittendorfer, A. Garhofer, J. Redinger, J. Klimeš, J. Harl, and G. Kresse, Phys. Rev. B **84**, 201401 (2011).

[17] T. Björkman, A. Gulans, A. V. Krasheninnikov, and R. M. Nieminen, Phys. Rev. Lett. **108**, 235502 (2012).

[18] L. Schimka, J. Harl, A. Stroppa, A. Gruneis, M. Marsman, F. Mittendorfer, and G. Kresse, Nat. Mater. **9**, 741 (2010).

[19] M. Macher, J. Klimeš, C. Franchini, and G. Kresse, J. Chem. Phys. **140**, 084502 (2014).

[20] S. Grimme, J. Comput. Chem. **27**, 1787 (2006).

[21] A. Tkatchenko and M. Scheffler, Phys. Rev. Lett. **102**, 073005 (2009).

[22] A. Tkatchenko, R. A. DiStasio, R. Car, and M. Scheffler, Phys. Rev. Lett. **108**, 236402 (2012).

[23] S. Grimme, Comp. M. Sci. **1**, 211 (2011).

[24] M. Dion, H. Rydberg, E. Schröder, D. C. Langreth, and B. I. Lundqvist, Phys. Rev. Lett. **92**, 246401 (2004).

[25] D. C. Langreth, M. Dion, H. Rydberg, E. Schroder, P. Hyldgaard, and B. I. Lundqvist, Int. J. Quantum Chem. **101**, 599 (2005).

[26] D. C. Langreth, B. I. Lundqvist, S. D. Chakarova-Käck, V. R. Cooper, M. Dion, P. Hyldgaard, A. Kelkkanen, J. Kleis, L. Kong, S. Li, P. G. Moses, E. Murray, A. Puzder, H. Rydberg, E. Schroder, and T. Thonhauser, J Phys.: Condens. Matter **21**, 084203 (2009).

[27] O. A. Vydrov and T. Van Voorhis, J. Chem. Phys. **133**, 244103 (2010).

[28] J. Klimeš and A. Michaelides, J. Chem. Phys. **137**, 120901 (2012).

[29] A. Grüneis, M. Marsman, J. Harl, L. Schimka, and G. Kresse, J. Chem. Phys. **131**, 154115 (2009).

[30] J. E. Bates and F. Furche, J. Chem. Phys. **139**, 171103 (2013).

[31] X. Ren, A. Tkatchenko, P. Rinke, and M. Scheffler, Phys. Rev. Lett. **106**, 153003 (2011).

[32] J. Paier, X. Ren, P. Rinke, G. E. Scuseria, A. Grüneis, G. Kresse, and M. Scheffler, New J. Phys. **14**, 043002 (2012).

[33] X. Ren, P. Rinke, V. Blum, J. Wieferink, A. Tkatchenko, A. Sanfilippo, K. Reuter, and M. Scheffler, New J. Phys. **14**, 053020 (2012).

[34] X. Ren, P. Rinke, G. E. Scuseria, and M. Scheffler, Phys. Rev. B **88**, 035120 (2013).

[35] T. Olsen and K. S. Thygesen, Phys. Rev. B **86**, 081103 (2012).

[36] P. Bleiziffer, A. Heßelmann, and A. Görling, J. Chem. Phys. **139**, 084113 (2013).

[37] J. Klimeš and G. Kresse, J. Chem. Phys. **140**, 054516 (2014).

[38] A. M. Burow, J. E. Bates, F. Furche, and H. Eshuis, J. Chem. Theory Comput. **10**, 180 (2014).

[39] J. Rekkedal, S. Coriani, M. F. Iozzi, A. M. Teale, T. Helgaker, and T. B. Pedersen, J. Chem. Phys. **139**, 081101 (2013).

[40] H. N. Rojas, R. W. Godby, and R. J. Needs, Phys. Rev. Lett. **74**, 1827 (1995).

[41] L. Steinbeck, A. Rubio, L. Reining, M. Torrent, I. White, and R. Godby, Comput. Phys. Commun. **125**, 105 (2000).

[42] S. L. Adler, Phys. Rev. **126**, 413 (1962).

[43] N. Wiser, Phys. Rev. **129**, 62 (1963).

[44] M. Kaltak, J. Klimeš, and G. Kresse, J. Chem. Theory Comput. (to be published).

[45] J. E. Moussa, J. Chem. Phys. **140**, 014107 (2014).

[46] M. Gell-Mann and K. A. Brueckner, Phys. Rev. **106**, 364 (1957).

[47] C. Møller and M. S. Plesset, Phys. Rev. **46**, 618 (1934).

[48] M. Marsman, A. Grüneis, J. Paier, and G. Kresse, J. Chem. Phys. **130**, 184103 (2009).

[49] A. Takatsuka, S. Ten-no, and W. Hackbusch, J. Chem. Phys. **129**, 044112 (2008).

[50] R. Martin, *Electronic Structure: Basic Theory and Practical Methods* (Cambridge University Press, Cambridge, UK, 2004).

[51] C. Kittel, *Introduction to Solid State Physics* (Wiley, Hoboken, NJ, 2004).

[52] G. Czycholl, *Theoretische Festkörperphysik: Von den klassischen Modellen zu modernen Forschungsthemen* (Springer, Berlin, 2007).

[53] P. E. Blöchl, Phys. Rev. B **50**, 17953 (1994).

[54] G. Kresse and D. Joubert, Phys. Rev. B **59**, 1758 (1999).

[55] M. Shishkin and G. Kresse, Phys. Rev. B **74**, 035101 (2006).

[56] M. Gajdoš, K. Hummer, G. Kresse, J. Furthmüller, and F. Bechstedt, Phys. Rev. B **73**, 045112 (2006).

[57] J. P. Perdew, K. Burke, and M. Ernzerhof, Phys. Rev. Lett. **77**, 3865 (1996); **78**, 1396 (1997).

[58] E. R. Batista, J. Heyd, R. G. Hennig, B. P. Uberuaga, R. L. Martin, G. E. Scuseria, C. J. Umrigar, and J. W. Wilkins, Phys. Rev. B **74**, 121102 (2006).

[59] D. Alfè, M. J. Gillan, M. D. Towler, and R. J. Needs, Phys. Rev. B **70**, 214102 (2004).

[60] R. G. Hennig, A. Wadehra, K. P. Driver, W. D. Parker, C. J. Umrigar, and J. W. Wilkins, Phys. Rev. B **82**, 014101 (2010).

[61] O. K. Al-Mushadani and R. J. Needs, Phys. Rev. B **68**, 235205 (2003).

[62] P. Rinke, A. Janotti, M. Scheffler, and C. G. Van de Walle, Phys. Rev. Lett. **102**, 026402 (2009).

[63] F. Corsetti and A. A. Mostofi, Phys. Rev. B **84**, 035209 (2011).

[64] W. Gao and A. Tkatchenko, Phys. Rev. Lett. **111**, 045501 (2013).

[65] F. Bruneval, Phys. Rev. Lett. **108**, 256403 (2012).

[66] M. I. J. Probert and M. C. Payne, Phys. Rev. B **67**, 075204 (2003).

[67] W. Parker, J. Wilins, and R. Hennig, Phys. Status Solidi B **248**, 267 (2011).

[68] W.-K. Leung, R. J. Needs, G. Rajagopal, S. Itoh, and S. Ihara, Phys. Rev. Lett. **83**, 2351 (1999).

[69] S. Chiesa, D. M. Ceperley, R. M. Martin, and M. Holzmann, Phys. Rev. Lett. **97**, 076404 (2006).

[70] A. Ural, P. B. Griffin, and J. D. Plummer, Phys. Rev. Lett. **83**, 3454 (1999).

[71] H. Bracht, N. A. Stolwijk, and H. Mehrer, Phys. Rev. B **52**, 16542 (1995).

[72] G. D. Watkins, ECS Proc. **99-1**, 38 (1999).

[73] D. Caliste and P. Pochet, Phys. Rev. Lett. **97**, 135901 (2006).